

Long-lived Giant Number Fluctuations in a Swarming Granular Nematic

Vijay Narayan,^{1*} Sriram Ramaswamy,^{1,2} Narayanan Menon³

¹CCMT, Department of Physics, Indian Institute of Science, Bangalore 560012, India

²CMTU, Jawaharlal Nehru Centre for Advanced Scientific Research, Bangalore 560064, India

³Department of Physics, University of Massachusetts, Amherst, MA 01003, USA

*To whom correspondence should be addressed; E-mail: vj@physics.iisc.ernet.in

Coherently moving flocks of birds, beasts or bacteria are examples of living matter with spontaneous orientational order. How do these systems differ from thermal equilibrium systems with such liquid-crystalline order? Working with a fluidized monolayer of macroscopic rods in the nematic liquid crystalline phase, we find giant number fluctuations consistent with a standard deviation growing linearly with the mean, in contrast to any situation where the Central Limit Theorem applies. These fluctuations are long-lived, decaying only as a logarithmic function of time. This shows that flocking, coherent motion and large-scale inhomogeneity can appear in a system in which particles do not communicate except by contact.

Density is a property that one can measure with arbitrary accuracy for materials at thermal equilibrium simply by increasing the size of the volume observed. This is because a region of

volume V , with N particles on average, ordinarily shows fluctuations with standard deviation $\Delta N \propto \sqrt{N}$, so that fluctuations in the number density go down as $1/\sqrt{V}$. Liquid-crystalline phases of active or self-propelled particles (1-4) are different, with ΔN predicted (2-5) to grow faster than \sqrt{N} , and as fast as N in some cases (5), making density an ill-defined quantity even in the limit of a large system. These predictions show that flocking, coherent motion and giant density fluctuations are intimately related consequences of the orientational order that develops in a sufficiently dense grouping of self-driven objects with anisotropic body shape. This has significant implications for biological pattern formation and movement ecology (6): the coupling of density fluctuations to alignment of individuals will affect populations as diverse as herds of cattle, swarms of locusts (7), schools of fish (8, 9), motile cells (10), and filaments driven by motor proteins (11-13).

We report here that persistent, giant number fluctuations and the coupling of particle currents to particle orientation arise in a far simpler driven system, namely, an agitated monolayer of rod-like particles shown in (14) to exhibit liquid-crystalline order. These fluctuations have also been observed in computer simulations of a simple model of the flocking of apolar particles by Chaté *et al.* (15). The rods we use are cut to a length $\ell = 4.6 \pm 0.16$ mm from copper wire of diameter $d = 0.8$ mm. The ends of the rods are etched to give them the shape of a rolling-pin. The rods are confined in a quasi-2-dimensional cell 1 mm tall and with a circular cross-section 13 cm in diameter. The cell is mounted in the horizontal plane on a permanent magnet shaker and vibrated vertically at a frequency $f = 200$ Hz, with an amplitude, A , between 0.025 and 0.043 mm. The resultant dimensionless acceleration $\Gamma = (4\pi^2 f^2 A)/g$, where g is the acceleration due to gravity, varies between $\Gamma = 4$ and $\Gamma = 7$. We vary the total number of particles in the cell, N_{total} between 1500 and 2820. N_{total} in each instance is counted by hand. The area fraction, ϕ , occupied by the particles is the total projected area of the all rods divided by the surface area of the cell. ϕ varies from 35% to 66%. Our experimental system is similar to those used to study

the phase behaviour of inelastic spheres (16, 17). Galanis *et al.* (18) shook rods in a similar setup, albeit with much less confinement in the vertical direction. The particles are imaged with a digital camera (**Data Acquisition** (19)).

The rods gain kinetic energy through frequent collisions with the floor and the ceiling of the cell. Since the axes of the particles are almost always inclined to the horizontal, these collisions impart or absorb momentum in the horizontal plane. Collisions between particles conserve momentum, but also drive horizontal motion by converting vertical motion into motion in the plane. Inter-particle collisions as well as particle-wall collisions are inelastic, and all particle motion would cease within a few collision times if the vibrations were switched off. The momentum of the system of rods is not conserved either, since the walls of the cell can absorb or impart momentum. The rods are apolar – individual particles do not have a distinct head and tail that determine fore-aft orientation or direction of motion – and can form a true nematic phase. The experimental system thus has all the physical ingredients of an active nematic (1-4).

The system is in a very dynamic steady state, with particle motion (see movie S1 (19)) organized in macroscopic swirls. Swirling motions do not necessarily imply the existence of giant number fluctuations (20, 21), however, particle motions in our system generate anomalously large fluctuations in density. Figure 1A shows a typical instantaneous configuration, and the inset to Fig. 1B shows the orientational correlation function $G_2(r) = \langle \cos 2(\theta_i - \theta_j) \rangle$, where i, j run over pairs of particles separated by a distance r and oriented at angles θ_i, θ_j with respect to a reference axis. The angle brackets denote an average over all such pairs and about 150 images spaced 15 seconds apart in time. The data in the inset show that the systems with $N_{total} = 2500$ and 2820 display quasi-long ranged nematic order, where $G_2(r)$ decays as a power of the separation, r . On the other hand, the system with $N_{total} = 1500$ shows only short-ranged nematic order, with $G_2(r)$ decaying exponentially with r . Details of the crossover between these two behaviours can be found in (**The Shaking Amplitude** Γ (19)). Autocorrelations of the density

field as well as of the orientation of a tagged particle decay to zero on much shorter time-scales (**Statistical Independence of Configurations Sampled** (19)), so we expect these images to be statistically independent. To quantify the number fluctuations, we extracted from each image the number of particles in subsystems of different size, defined by windows ranging in size from $0.1 \times 0.1 \ell^2$ to $12 \times 12 \ell^2$. From a series of images we determined, for each subsystem size, the average N and the standard deviation, ΔN , of the number of particles in the window. For any system in which the number fluctuations obey the conditions of the Central Limit Theorem (22), $\Delta N/\sqrt{N}$ should be a constant, independent of N . Figure 1B shows that when the area fraction ϕ is large, $\Delta N/\sqrt{N}$ is not a constant. Indeed, for big enough subsystems, the data show giant fluctuations, ΔN , in the number of particles, growing far more rapidly than \sqrt{N} and consistent with a proportionality to N . For smaller average number density, where nematic order is poorly developed, this effect disappears, and $\Delta N/\sqrt{N}$ is independent of N , as in thermal equilibrium systems. The roll-off in $\Delta N/\sqrt{N}$ at the highest values of N is a finite-size effect: for subsystems that approach the size of the entire system, large number fluctuations are no longer possible since the total number of particles in the cell is held fixed.

We examine a subsystem of size $\ell \times \ell$ (i.e., one rod length on a side) and obtain a time-series of particle number, $N(t)$, by taking images at a frame rate of 300 frames/sec. From this we determine the temporal autocorrelation, $C(t)$, of the density fluctuations. As shown in Fig. 2, $C(t)$ decays logarithmically in time, unlike the much more rapid t^{-1} decay of random, diffusively relaxing density fluctuations in two dimensions. Thus the density fluctuations are not only anomalously large in magnitude but also extremely long-lived. Indeed, these two effects are intimately related: an intermediate step in the theoretical argument (5) that predicts giant number fluctuations shows that density fluctuations at a wavenumber q have a variance proportional to q^{-2} and decay diffusively. This leads to the conclusion (**Long-lived Density Autocorrelation** (19)) that in the time regime intermediate between the times taken for a density mode to diffuse

a particle length and the size of the system, the autocorrelation function of the local density decays only logarithmically in time. While the observations agree with the predicted logarithmic decay, we cannot as yet make quantitative statements about the coefficient of the logarithm. It is important to note that the size of subsystem is below the scale of subsystem size at which the standard deviation has become proportional to the mean. In flocks and herds as well, measuring the dynamics of local density fluctuations will yield crucial information regarding the entire system's dynamics, and can be used to test the predictions of Toner and Tu (2,3).

What are the microscopic origins of the giant density fluctuations? Both in active and in equilibrium systems, particle motions lead to spatial variations in the nematic ordering direction. However, in active systems alone, such bend and splay of the orientation are predicted (5) to select a direction for coherent particle currents. These curvature-driven currents in turn engender giant number fluctuations. We find qualitative evidence for curvature-induced currents in the flow of particles near topological defects (**Curvature-Induced Mass Flow (19)**). In the apolar flocking model of (15) particles move by hopping along their axes and then re-orienting, with a preference to align parallel to the average orientation of particles in their neighbourhood. Requiring that the hop be along the particle axis was sufficient to produce giant number fluctuations in the nematic phase of the system. It was further suggested in (15) that the curvature-induced currents of (5), although not explicitly put into their simulation, must emerge as a macroscopic consequence of the rules imposed on microscopic motion. This suggestion is substantiated by the work of Ahmadi *et al.* (23) who start from a microscopic model of molecular motors moving preferentially along biofilaments and show by coarse-graining this model that the equation of motion for the density of filaments contains precisely the term in (5) responsible for curvature-induced currents.

In our experiments we find anisotropy at the most microscopic level of single particle motion, even at time scales shorter than the vibration frequency f . In equilibrium, the mean kinetic

energy associated with the two in-plane translation degrees of freedom of the particle are equal, by the equipartition theorem, even if the particle shape is anisotropic. Figure 3 is a histogram of the magnitude of particle displacements over a time corresponding to the camera frame rate ($1/300$ sec, or $\frac{2}{3}f^{-1}$). The displacement along and perpendicular to the axis of the rod are displayed separately, showing that a particle is about 2.3 times as likely to move along its length as it is to move transverse to its length. Since the period of the imposed vibration (f^{-1}) sets the scale for the mean free time of the particles, this shows that the motion of the rods is anisotropic even at time scales less than or comparable to the mean free time between collisions.

We have thus presented an experimental demonstration of giant, long-lived, number fluctuations in a 2-dimensional active nematic. The particles in our driven system do not communicate except by contact, have no sensing mechanisms and are not influenced by the spatially-varying pressures and incentives of a biological environment. This reinforces the view that in living matter as well, simple, non-specific interactions can give rise to large spatial inhomogeneity. Equally important, these effects offer a counterexample to the deeply held notion that density is a sharply-defined quantity for a large system.

References and Notes

1. T. Vicsek, A. Czirok, E. Ben-Jacob, I. Cohen, O. Shochet, *Phys. Rev. Lett.* **75**, 1226 (1995).
2. J. Toner, Y. Tu, *Phys. Rev. Lett.* **75**, 4326 (1995).
3. J. Toner, Y. Tu, *Phys. Rev. E* **58**, 4828 (1998).
4. J. Toner, Y. Tu, S. Ramaswamy, *Ann. Phys.* **318**, 170 (2005).
5. S. Ramaswamy, R. A. Simha, J. Toner, *Europhys. Lett.* **62**, 196 (2003).
6. C. Holden, *Science* **313**, 779 (2006).
7. J. Buhl *et al.*, *Science* **312**, 1402 (2006).
8. N. Makris *et al.*, *Science* **311**, 660 (2006).
9. C. Becco *et al.*, *Physica A*, **367**, 487 (2006).
10. B. Szabó *et al.*, *Phys. Rev. E* **74**, 061908 (2006).
11. F. Nédélec, T. Surrey, A. C. Maggs, S. Leibler, *Nature* **389**, 305 (1997).
12. D. Bray, *Cell Movements: From Molecules to Motility* (Garland Publishing, New York, 2001).
13. H. Gruler, U. Dewald, M. Eberhardt, *Eur. Phys. J. B* **11**, 187 (1999).
14. V. Narayan, N. Menon, S. Ramaswamy, *J. Stat. Mech.* (2006) P01005
15. H. Chaté, F. Ginelli, R. Montagne, *Phys. Rev. Lett.* **96**, 180602 (2006).
16. A. Prevost, D. A. Egolf, J. S. Urbach, *Phys. Rev. Lett.* **89**, 084301 (2002).
17. P. M. Reis, R. A. Ingale, M. D. Shattuck, *Phys. Rev. Lett.* **96**, 258001 (2006).
18. J. Galanis, D. Harries, D. L. Sackett, W. Losert, R. Nossal, *Phys. Rev. Lett.* **96**, 028002 (2006).

19. Supporting Online Material

www.sciencemag.org

Materials and Methods

SOM Text

Figs. S1, S2, S3, S4, S5, S6

Movie S1, S2

20. D. L. Blair, T. Neicu, A. Kudrolli, *Phys. Rev. E* **67**, 031303 (2003).

21. I. Aranson, D. Volfson, L. S. Tsimring, *Phys. Rev. E* **75**, 051301 (2007).

22. W. Feller, *An introduction to Probability Theory and its Applications, Volume I*, (John Wiley & Sons, New York, 3rd edition, 2000)

23. A. Ahmadi, T. B. Liverpool, M. C. Marchetti, *Phys. Rev. E* **74**, 061913 (2006).

1. **Acknowledgements.** We thank V. Kumaran, P. Nott and A. K. Raychaudhuri for generously letting us use their experimental facilities. VN thanks Sohini Kar for help with some of the experiments. VN and SR respectively thank the Council for Scientific and Industrial Research, India and the Indo-French Centre for the Promotion of Advanced Research (grant 3504-2) for support. The Centre for Condensed Matter Theory is supported by the Department of Science and Technology, India. NM acknowledges financial support from the National Science Foundation under NSF-DMR 0606216 and 0305396.

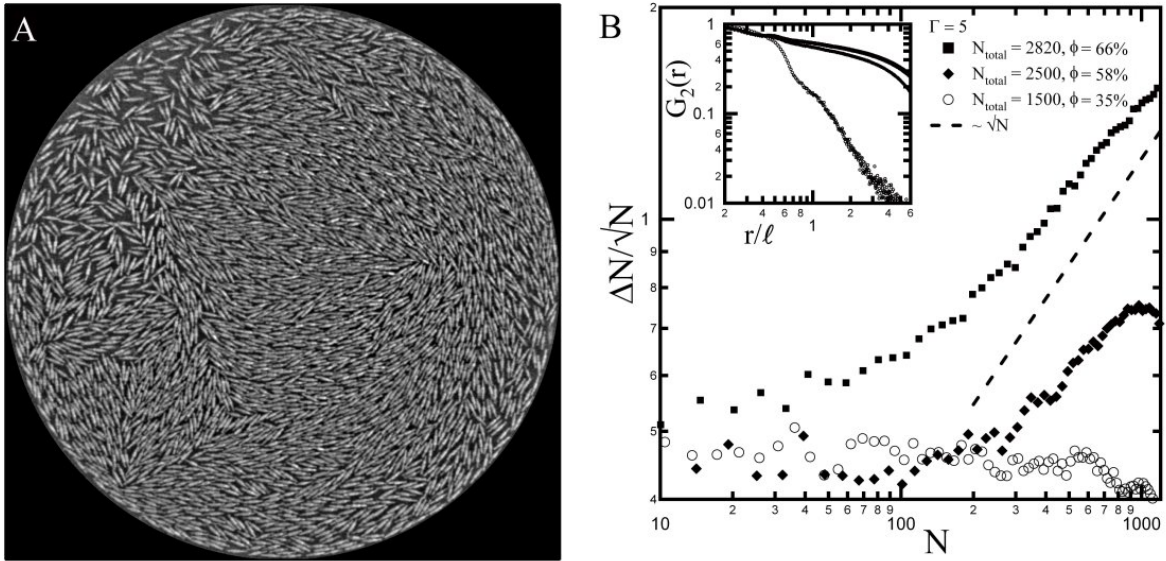


Figure 1: Giant number fluctuations in active granular rods. A) shows a snapshot of the nematic order assumed by the rods. There are 2820 particles (counted by hand) in the cell (area fraction 66%), being sinusoidally vibrated perpendicular to the plane of the image, at a peak acceleration of $\Gamma = 5$. The sparse region at the top between 10 and 11 o'clock is an instance of a large density fluctuation. These take several minutes to relax and form elsewhere. B) shows the magnitude of the number-fluctuations (quantified by ΔN , the standard deviation, normalized by the square root of the mean number, N) against the mean number of particles, for subsystems of various sizes. The number fluctuations in each subsystem are determined from images taken every 15 seconds over a period of 40 minutes (**Methods** (19)). The squares represent the system shown in A. It is a dense system where the nematic order is well developed. The magnitude of the scaled number fluctuations decreases in more dilute systems, where the nematic order is weaker (**The Shaking Amplitude** Γ (19)). Deviations from the Central Limit Theorem result are still visible at an area fraction $\simeq 58\%$ (diamonds), but not at an area fraction $\simeq 35\%$ (circles). The inset shows the nematic-order correlation function as a function of spatial separation.

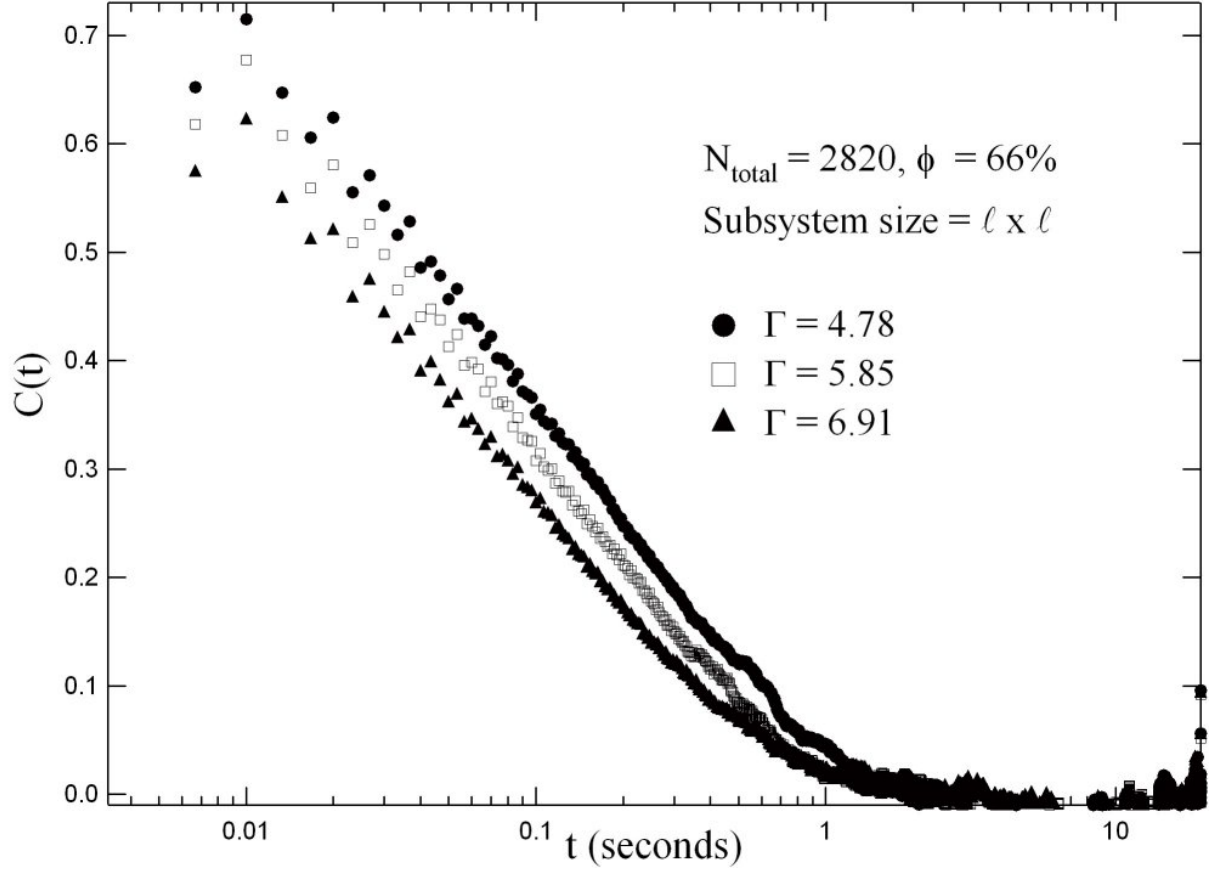


Figure 2: The logarithmic dependence of the local density autocorrelation $C(t) = \langle \varphi(0)\varphi(t) \rangle$ ($\varphi(t)$ is the deviation from the mean of the instantaneous number density of particles) is a direct consequence (**Long-lived Density Autocorrelation (19)**), and hence a clear signature, of the large density fluctuations in the system. It is remarkable that such a local property reflects the dynamics of the entire system so strongly. It is seen that increasing Γ shortens the decay time. This is consistent with the fact that the magnitude of the giant number fluctuations grows with the nematic order (**The Shaking Amplitude Γ (19)**).

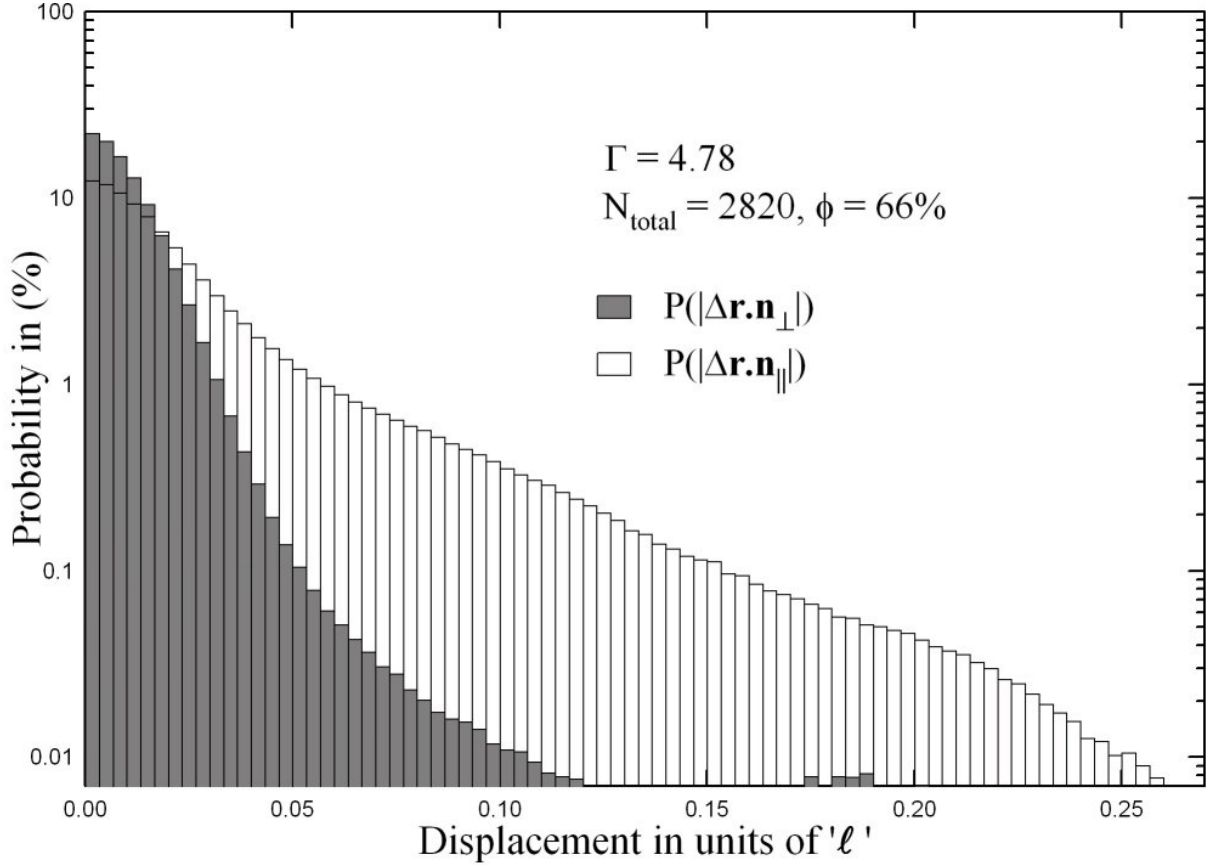


Figure 3: The microscopic origin of the macroscopic density fluctuations. The probability distribution of the magnitude of the displacement along and transverse to the particle's long axis over an interval of $1/300$ of a second shows that short time motion of the rods is anisotropic even at the time-scale of the collision time. This anisotropy is explicitly forbidden in equilibrium systems by the equipartition theorem.

Supporting Online Material

Methods

Data Acquisition

To study the instantaneous spatial configurations of the system, we used a digital camera (Canon PowerShot G5) at a resolution of 2592x1944 pixels. Images of the entire cell were taken at roughly 15-second intervals from which we extracted the position and orientation of all particles (details of the image analysis are given in the section **Image Analysis**). The degree of orientational order was quantified by the nematic order correlation function

$$G_2(r) = \langle \sum_{i,j} \cos[2(\theta_i - \theta_j)] \rangle$$

Here the labels i, j run over all pairs of particles with separation r , and the angular brackets represent an average over the images. Movie S1 was made from images taken using this camera (see section **Description of the Movie material**).

In order to probe the dynamics of the system, we used a high speed camera (Phantom v7) to track particles in a region of the entire sample consisting of 400 - 500 particles. Images were taken at 300 frames per second for a period of 20 seconds and at a resolution of 800x600 pixels. Movie S2 was made using this camera (see section **Description of the Movie material**).

Image Analysis

The centre-of-mass coordinates and orientation of all the particles were extracted from each image by image analysis routines. Particle identification in the image analysis was complicated by the high number density of particles and the consequent overlaps in particle footprints. Further-

more, the particles are of unusual shape and not perfectly monodisperse. The image analysis was done using the ImageJ program. To separate particles that were in contact, the contrast at the edges of the particles was enhanced, followed by a sequence of erosion and opening operations. Typically 90% of the particles were identified using this procedure. Two further special cases had to be dealt with for the remaining particles. The first was that erosion often caused the narrow ends of the particles to detach, yielding spurious identification as individual particles. To eliminate them, we imposed both a minimum-area threshold as well as a condition that eliminated the smaller of a pair of particles if they were lying too close in the longitudinal direction. The second class of problem came from particle footprints whose tips fused together forming a composite particle along their length. These cases were easy to identify both by their large area and their long aspect ratio. We resolved such cases by assigning to the composite object, two particles lying symmetrically about the original position along the original axis. They were assigned the same orientation as the originally identified object.

When analysing data to study statics, the focus was on identifying each particle in the system. Since we were trying to quantify the fluctuations in the number density, it was imperative that no spurious number fluctuations arose from the image analysis. Both direct visual verification of the accuracy of the identification and the roll-off in Fig. 1B assure us that the fluctuations due to errors in the image analysis are much smaller than the inherent number fluctuations in the system.

When studying the dynamics of the particles, we developed a standard particle-tracking code based on a minimum distance criterion between particles in successive frames. This approach was effective because particles typically moved only about a fiftieth of their length between successive images. If no particle was found in a later frame that uniquely corresponded to the initial one, the particle location was held for comparison to later images, so that a particle “lost” in a particular frame might be recovered later.

Curvature-Induced Mass Flow

In reference (S1) the authors argue that curvature in the nematic orientation gives rise to mass motion of particles, and that the great abundance and slow decay of large-scale curvature leads ultimately to giant number fluctuations. To get direct evidence of this mechanism in our experiment would require mapping out the curvature field and correlating it to the local mass flux. For simplicity, we look instead for individual instances of large curvature and the corresponding motion. This is conveniently done by focusing on the regions around topological defects in an otherwise well-oriented nematic. Two types of defects, strength $+1/2$ and $-1/2$, are seen with their associated nematic director fields shown in Fig. S1. A topological defect is a localized imperfection in the state of order which cannot be removed by continuous deformations of the order parameter. For a more detailed understanding of defects in nematics see reference (S2). What is crucial for our discussion is that the orientation field around the $+1/2$ defect in figure B is polar and breaks the fore-aft symmetry, while that around the $-1/2$ defects is three-fold symmetric. A curvature-induced drift mechanism would result in particle motion in the directions indicated by the arrows in figures A and B. The symmetry of the field around the strength $-1/2$ defect will result in no net motion, while the curvature around the $+1/2$ defect has a well-defined polarity and hence should move in the direction of its “nose” as shown in the figure. Movie S2, stills from which are seen in Fig. S1, shows precisely this behaviour.

The Shaking Amplitude Γ

Γ , the dimensionless acceleration, is one of the 2 quantities we vary to explore our parameter space, the other being density. Naïvely one would expect that Γ in our nonequilibrium phase diagram is analogous to the temperature in thermal equilibrium systems – the harder one shakes the system, the more disordered it gets, making a direct correspondence with the temperature.

We observe a more complicated, non-monotonic trend.

Figure S2 shows the nematic order in the system as a function of density and Γ . Increasing density clearly increases nematic order. At the three lowest densities, increasing Γ increases the nematic order. At $N_{total} = 2820$ however, increasing Γ decreases the nematic order. The crossover in the behaviour occurs at $N_{total} = 2500$ where we see that $G_2(r)$ for $\Gamma = 5$ and $\Gamma = 6$ are nearly indistinguishable. Put together, this suggests that these points are near a re-entrant portion of the isotropic-nematic transition.

The complicated role Γ plays in the system's dynamics is apparent even in the giant number fluctuations. Figure S3 shows $\Delta N/\sqrt{N}$ as a function of N for 4 different densities. We see that there are two regimes of fluctuations, most clearly distinguishable in the $N_{total} = 2500$ curve: (i) $\Delta N \propto \sqrt{N}$ at small N , and (ii) $\Delta N \propto N$, the giant fluctuations, at large N . The \sqrt{N} at smaller N arises from uncorrelated short-time diffusion of particles and exists even in the isotropic phase. The giant fluctuations dominate, as expected from (S1), at large N , and should be larger in systems with stronger nematic order. And indeed, increasing density (and hence the nematic order) suppresses the \sqrt{N} -fluctuations and enhances the N -fluctuations, as is seen in the $N_{total} = 2000$ and $N_{total} = 2500$ curves in Fig. S3. At lower subsystem sizes the \sqrt{N} -fluctuations will dominate. Since these are stronger for dilute systems, the magnitude of fluctuations is greater for $N = 2000$. For large enough subsystems, the contribution scaling as N , peculiar to the active nematic, will overwhelm the component that grows as \sqrt{N} . The $N_{total} = 2500$ curve shows a sharper rise than the $N_{total} = 2000$ curve and ultimately the fluctuations in the former outgrow those in the latter system.

To verify whether increased nematic order does indeed increase the magnitude of fluctuations, we plot $\Delta N/\sqrt{N}$ as a function of N for 2 different values of Γ in Fig. S4. As expected in the dilute systems, where Γ increases the nematic order, it increases the magnitude of fluctuations, whereas for $N_{total} = 2820$, increasing Γ reduces the magnitude of fluctuations. This

suggests that Γ sets the scale of two different stochastic processes at the level of an individual rod – fore-aft motion, which promotes nematic order, and rotational motion, which disrupts it.

Long-lived Density Autocorrelation

The principal result described in (S1) is that density modulations at long-wavelength $\lambda = 2\pi/q$ in active nematics have a variance proportional to q^{-2} , i.e., at larger and larger length scales, the system shows larger and larger statistical inhomogeneities. Defining $\varphi(\mathbf{r}, t) \equiv \rho(\mathbf{r}, t) - \rho_0$ where $\rho(\mathbf{r}, t)$ is the density at \mathbf{r} at time t and ρ_0 its time average, the prediction is that the static structure factor $S(\mathbf{q}) \equiv (1/\rho_0) \int_{\mathbf{r}} e^{i\mathbf{q}\cdot\mathbf{r}} \langle \varphi(\mathbf{0})\varphi(\mathbf{r}) \rangle \propto 1/q^2$. Converting to real space, the standard deviation ΔN would therefore grow as $N^{\frac{1}{2} + \frac{1}{d}}$ in d space dimensions. In 2 dimensions, thus, $\Delta N \propto N$: fluctuations grow linearly with the mean.

Dynamics

This global result has a sharp signature in the dynamics and statistics of the number of particles in a local region, as measured by the local density autocorrelation function

$$C(t) = \langle \varphi(\mathbf{x}, 0)\varphi(\mathbf{x}, t) \rangle. \quad (1)$$

For independently diffusing Brownian particles

$$C(t) = \int \frac{d^d q}{(2\pi)^d} e^{-q^2 D t} \sim t^{-d/2} \quad (2)$$

so that the local density autocorrelation function for a two-dimensional thermal equilibrium system of non-interacting Brownian particles decays as t^{-1} . This holds even for a diffusing density field coupled to the director field in a nematic liquid crystal at thermal equilibrium. For

an active nematic, however, as shown in (S1), Eq. (2) has to be modified to account for the anomalous q^{-2} abundance of the Fourier modes of the density at small wavenumber:

$$C(t) \sim \int_{2\pi/L}^{2\pi/a} dq q^{d-1} \frac{e^{-q^2 Dt}}{q^2} \quad (3)$$

with limits of integration determined by the coarse-graining scale a that we use to define the density, and the system-size L . This implies that for timescales between those corresponding to a and to L , $C(t)$ should decay as $\ln(L^2/Dt)$. Our experimental results are consistent with such a decay. We also find that coefficient of this logarithm depends on the coarse-graining scale a (Fig. S5).

The Statistical Independence of Configurations Sampled

To verify whether the images taken at 15-second intervals were indeed statistically independent, we calculated two quantities: 1) the local density autocorrelation $C(t)$ (discussed in section **Dynamics**) and 2) the autocorrelation of the orientation of a tagged particle, $C_\theta(t) = \langle \cos[2\{\theta(0) - \theta(t)\}] \rangle$. The angular brackets denote an average over all particles. Figure S6 shows that after an initially slow decay, for about a tenth of a second, C_θ decays logarithmically to zero as in two-dimensional thermal equilibrium nematics. This decay is over about 10 seconds. Thus, both $C_\theta(t)$ and $C(t)$ decay fast enough for us to be certain that the configurations we are sampling are statistically independent.

Description of the Movie Material

Movie S1 is a recording of a typical experimental run. The system is characterised by large inhomogeneities and large mass-fluxes. The system contains 2,820 ($\phi \simeq 66\%$) particles and is

being agitated at $\Gamma = 5$. The time is indicated at the bottom-left in minutes:seconds.

Movie S2 zooms into a small region of the sample. In particular, it compares the behaviour of $+1/2$ and $-1/2$ defects. A strength $+1/2$ defect is seen to move across the field of view of the camera starting at the bottom-left and the strength $-1/2$ defect is seen to remain relatively stationary as is argued in the section **Curvature-Induced Mass Flow**. The time is indicated in seconds at the bottom-left.

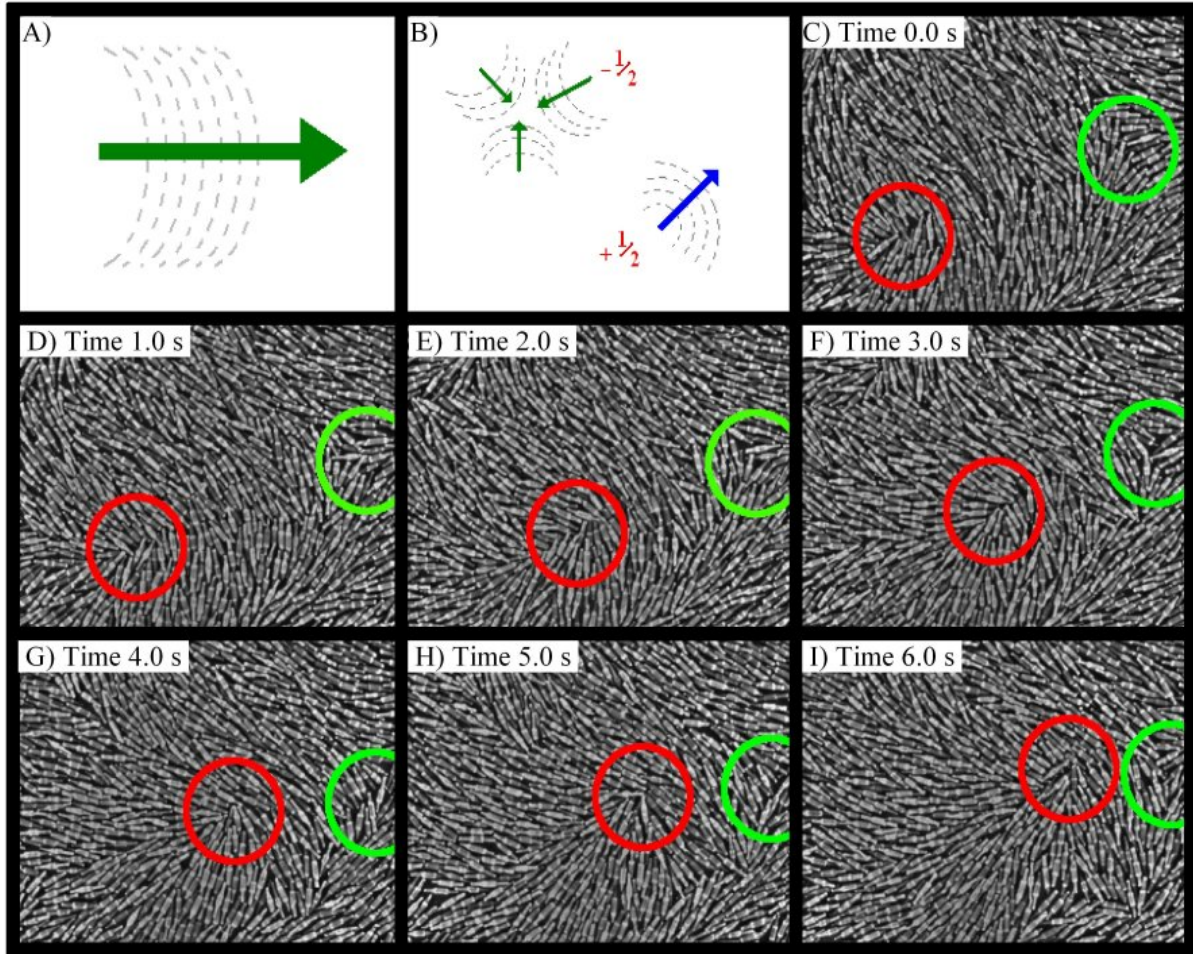


Figure S1. Schematic image A) shows the the motion predicted (S1) to arise in response to a curvature in the nematic director field. Fig B) applies this idea to the director fields around topological defects of strength $+1/2$ and $-1/2$. Particle orientations are shown in grey and the resulting particle currents are in the direction of the arrow. In B) the three competing particle streams would hold a $-1/2$ defect stationary whereas the $+1/2$ would move along the blue arrow. The time-lapse images C) through I) show exactly this behaviour in our experiment. The strength $-1/2$ defect (in the green circle) moves very little, while the strength $+1/2$ defect (encircled in red) moves substantially and systematically along its nose.

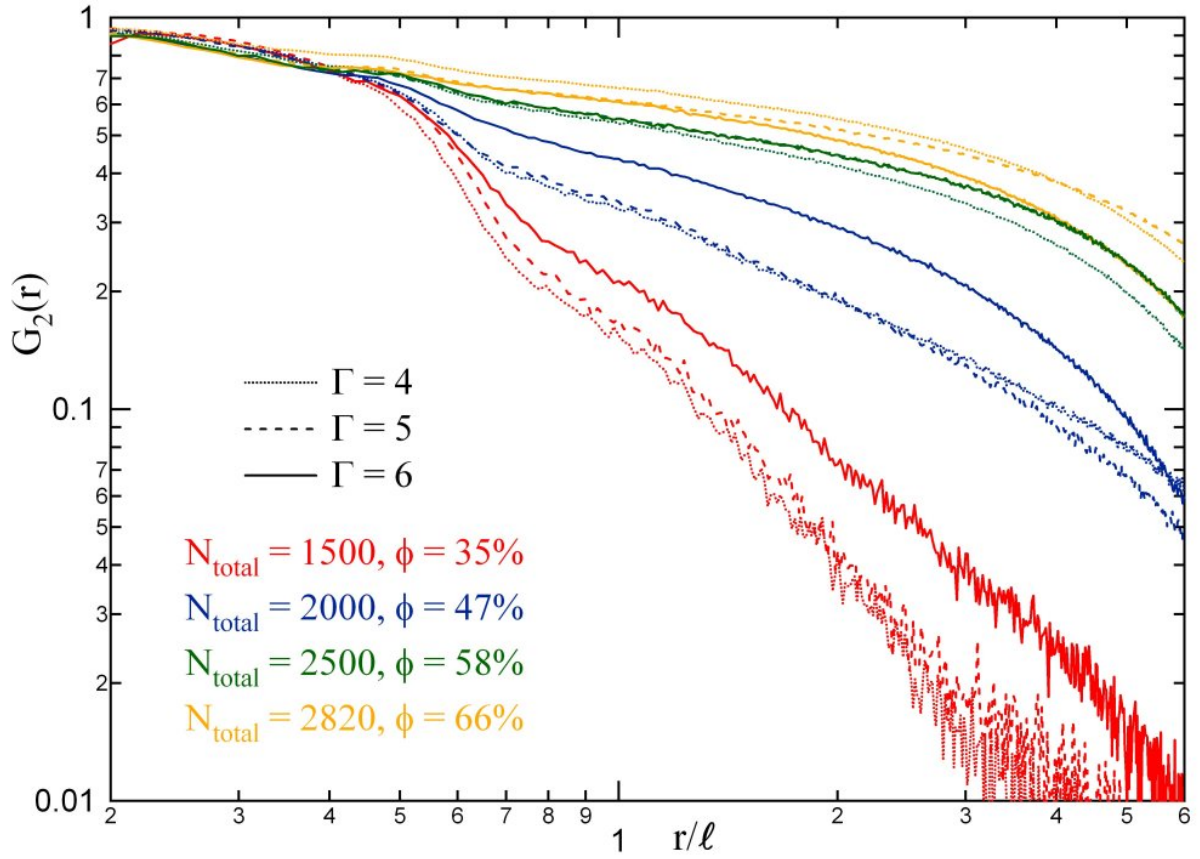


Figure S2. The nematic correlation function $G_2(r)$ for various values of Γ and density. The curves for $N_{\text{total}} = 2500$ at $\Gamma = 5$ and 6 cannot be distinguished at our resolution and, we believe, pass close to the isotropic-nematic transition.

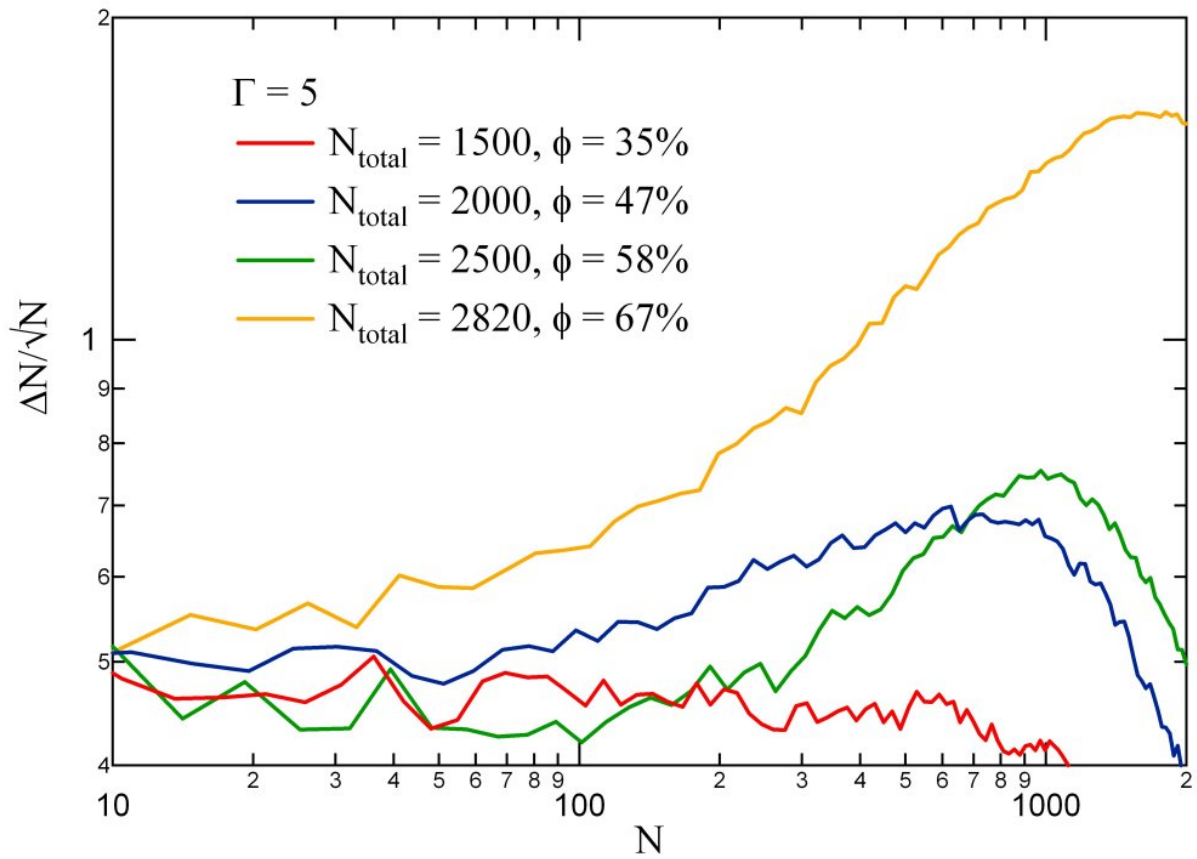


Figure S3. Number fluctuations at different densities: the magnitude of the density fluctuations grows with increasing nematic order.

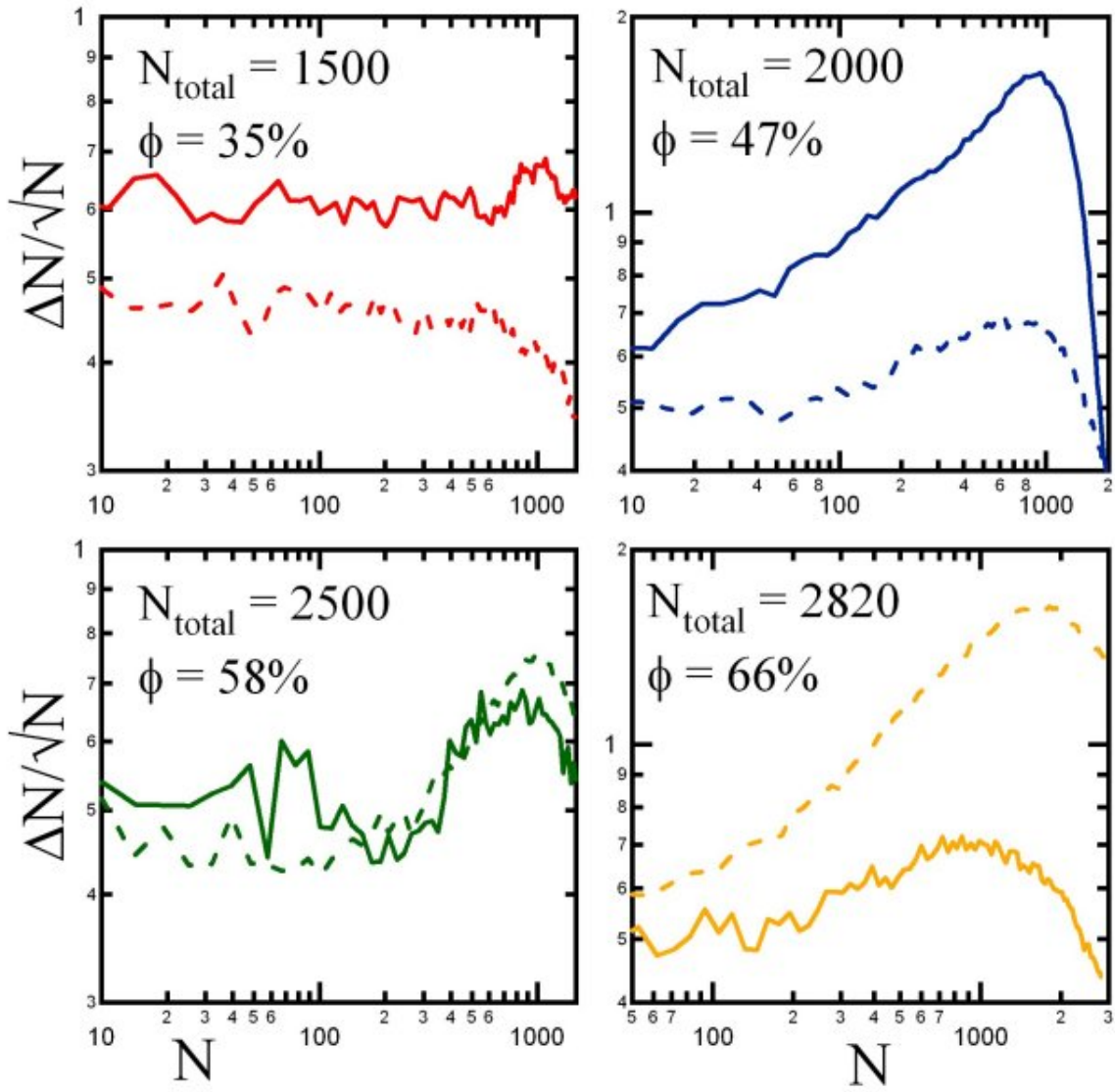


Figure S4. The dependence of the magnitude of relative density fluctuations on Γ . The dashed curves represent $\Gamma = 5$ and the solid curves $\Gamma = 6$.

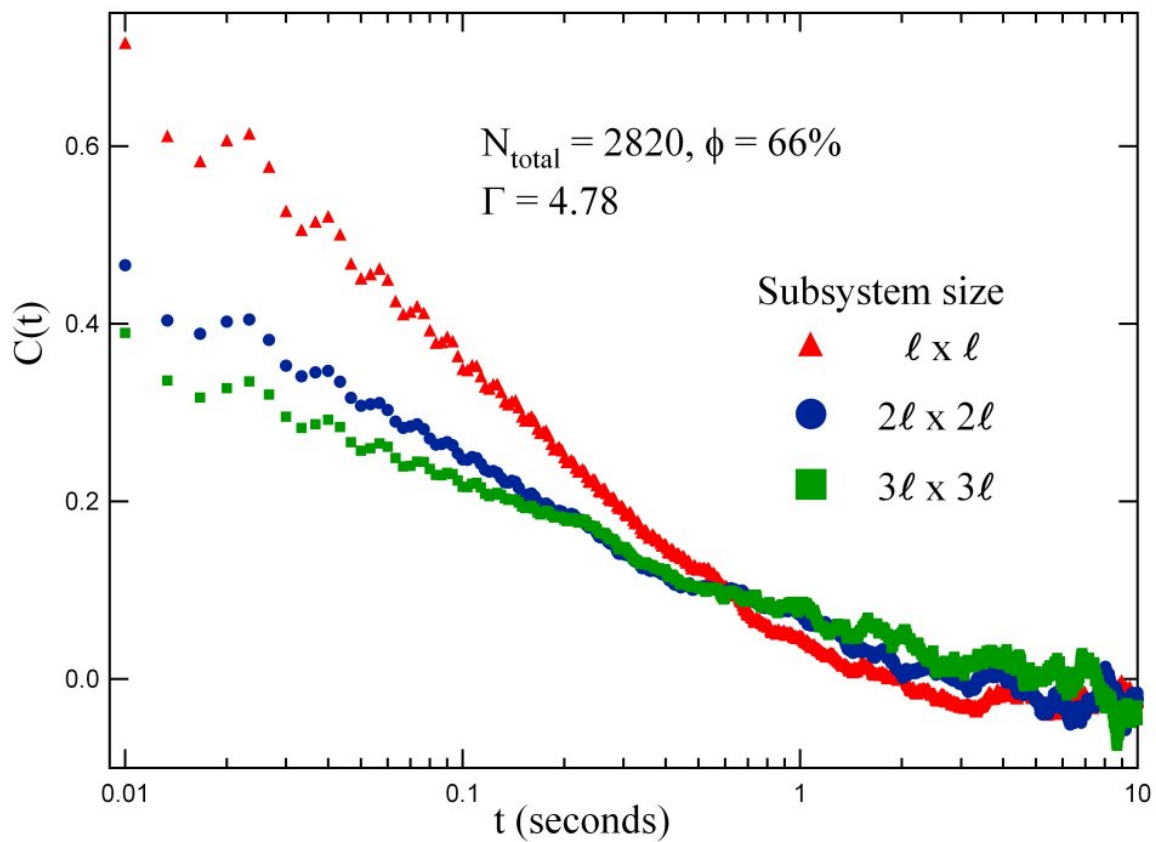


Figure S5. The figure shows $C(t)$ evaluated using for three different subsystems of linear size, a . The data for the two larger subsystem sizes has been scaled up by the subsystem area to facilitate viewing.

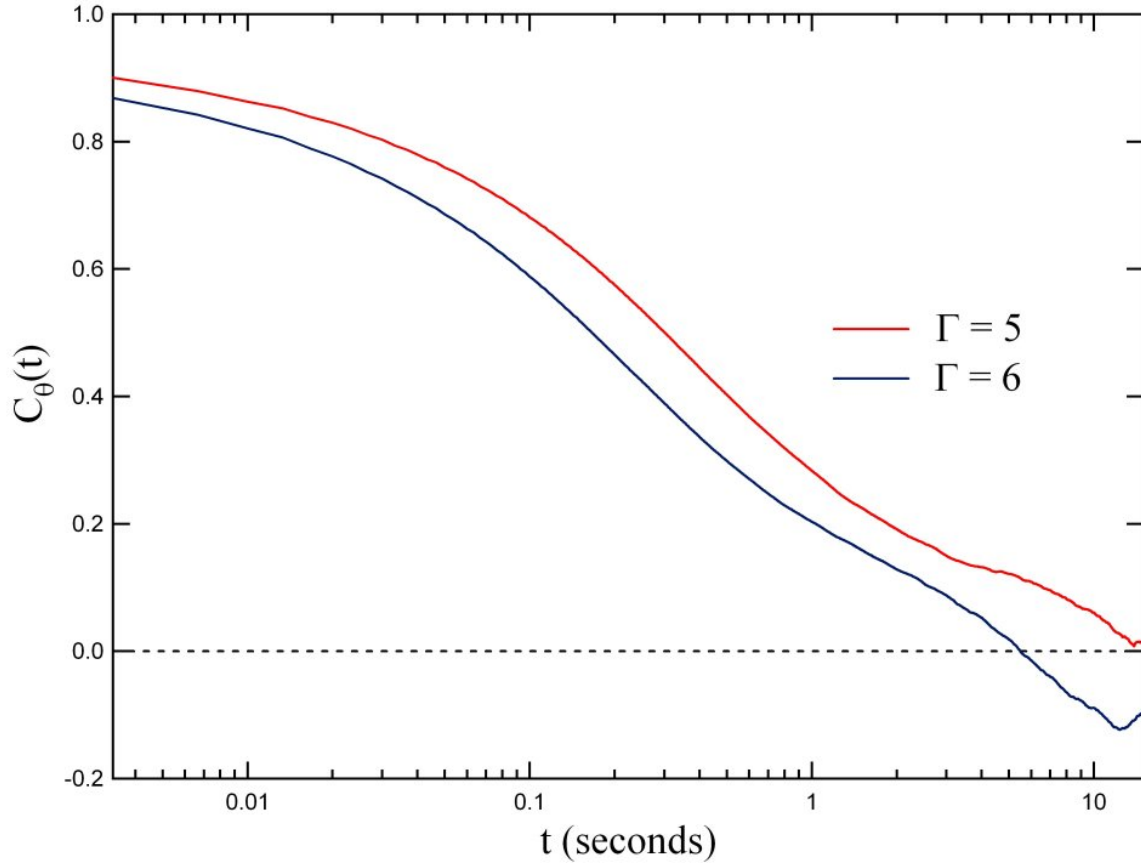


Figure S6. The autocorrelation of the orientation of a tagged particle, $C_{\theta}(t) = \langle \cos[2\{\theta_i(\tau) - \theta_i(\tau + t)\}] \rangle_{i,\tau}$ where i runs over all particles.

References

- S1.** S. Ramaswamy, R. A. Simha, J. Toner, *Europhys. Lett.* **62**, 196 (2003).
S2. P. G. de Gennes, J. Prost, *The Physics of Liquid Crystals*, Clarendon, (Clarendon, Oxford 1993); chap. 4, p. 169